The role of off-highway vehicle activity in augmenting dust emissions at the Oceano Dunes State Vehicular Recreation Area, Oceano, CA

J.A. Gillies [a,*], E. Furtak-Cole [a], G. Nikolich [b], V. Etyemezian [b]

[a] *Division of Atmospheric Sciences, Desert Research Institute, Reno, Nevada, USA*
[b] *Division of Atmospheric Sciences, Desert Research Institute, Las Vegas, Nevada, USA*

ARTICLE INFO

ABSTRACT

The Oceano Dunes State Vehicular Recreation Area (ODSVRA) allows off-highway vehicle (OHV) activity on this coastal dune system. Three sources of data were examined to determine if OHV activity increased wind-blown dust emissions originating from the ODSVRA. Measurements of emissivity (mg m^{-2} s^{-1}) of particulate matter (PM) from dune sands were made using the PI-SWERL® instrument from 2013 through to 2020 in the area with OHV activity and in areas where OHV access is not permitted. These measurements indicated that the mean emissivity of the riding area was two to three times higher than the mean of the non-riding areas, for wind shear velocity (u_*, m s^{-1}) conditions well-above threshold ($u_* > 0.5$ m s^{-1}). Measurements of Wind Power Density (WPD, W m^{-2}) and suspended particulate matter (PM, µg m^{-3}) at monitoring stations in the riding areas and downwind of the riding areas made between May and September 2019 indicate that PM concentrations increased 12% per month for similar WPD conditions. In 2020, OHV activity was prohibited beginning in March due to the SARS-CoV-2 pandemic. Network measurements of PM and WPD, April to August 2020 indicated a 12% decrease in PM concentrations per month for similar WPD conditions, suggesting the cessation of OHV activity resulted in the dunes becoming less emissive through time. Measurements of wind speed and suspended PM at a monitoring station downwind of a dune preserve area (no OHV activity allowed) for 2019 and 2020 indicate that PM and WPD measurements do not follow the same temporal trends for the in-Park and downwind of riding area influenced area stations, further suggesting that OHV activity influences dune emissivity.

1. Introduction

The Oceano Dunes in San Luis Obispo County, California is a known source of fugitive dust emissions (Gillies et al., 2017; Huang et al., 2019). Under conditions of elevated wind speed, exceedances of the US Federal standard (150 µg m^{-3}) and the State of California standard (50 µg m^{-3}) for 24-h mean concentrations of particulate matter ≤10 µm aerodynamic diameter (PM$_{10}$) have been observed. The Oceano Dunes is a Quaternary age coastal dune complex (Orme and Tchakerian, 1986) in California (Fig. 1), which contains the Oceano Dunes State Vehicular Recreation Area (ODSVRA) California State Park. The Park consists of ≈500 ha of dune environment that allows off highway recreational vehicle (OHV) activity as well as ≈280 ha of dune preserve that does not allow vehicle access. For winds >8 m s^{-1} with a dominant westerly component as measured 10 m above ground level (AGL), the threshold for sand transport is exceeded and this is accompanied by dust emissions (Gillies et al., 2017; Mejia et al., 2019; Huang et al., 2019).

Dune systems have been identified as sources of dust and mechanisms of dust production have been presented in the literature. Mechanisms for the creation of the fine dust particles that are emitted during active saltation of dune sand include abrasion by particle-to-particle impacts that spall dust-sized particles (Kuenen, 1960; Bristow and Moller, 2018; Swet et al., 2019), or by particle-to-particle collisions that remove clay coatings (Bullard et al., 2004, 2007; Bullard and White, 2005; Swet et al., 2020). At the Oceano Dunes, Huang et al. (2019) suggested both mechanisms occur with abrasion of feldspar grains and removal of clay coatings on quartz sand grains.

The ODSVRA dune environment is also one in which OHV activity exerts mechanisms of anthropogenic influence on the dunes throughout the area designated for active riding. The mechanisms consist of rotating vehicle tires that: 1) create a shearing force between sand particles at and near the surface, 2) mix the surface layer of sand, and 3) displace sand particles away from the path of vehicle travel. We hypothesize that these three mechanisms (and perhaps other unidentified near-surface

---

mechanisms) related to OHV activity have the potential to augment the emissivity of the dune sand creating higher concentrations of dust in the air than would occur if this dune system was not impacted by OHV activity. Surface disturbance by vehicle activity is well-known to increase dust emissions in desert environments (e.g., Wilshire and Nakata, 1976; Goossens and Buck, 2009a, 2009b, 2011).

To test the hypothesis, we draw on three sources of data. The first is a record of measurements of emissivity (mg m^{-2} s^{-1}) of PM$_{10}$ that have been made annually at the ODSVRA using the PI-SWERL® instrument (Etyemezian et al., 2007, 2014; Goossens et al., 2012; von Holdt et al., 2019) from 2013 through to 2020 in the area with OHV activity and in areas where OHV access is not permitted. The second source of data is derived from a network of stations located within and downwind of the area designated for OHV activity that measure meteorological parameters and the size distribution of suspended particulate matter. This network has operated annually, typically from April/May to September/October from 2017 through to 2020. The third source of data are from a monitoring station operated by the San Luis Obispo County Air Pollution Control District that is positioned downwind of the southern dune preserve (Oso Flaco). This station operates a Beta Attenuation Monitor (BAM) to measure concentrations of PM$_{10}$ as well as instruments that measure wind speed and direction.

In March 2020, a unique opportunity arose wherein the ODSVRA was closed to camping and OHV activity due to the SARS-CoV-2 pandemic. Within several weeks following the cessation of OHV activity measurement campaigns were initiated to repeatedly collect surface emissivity data using the PI-SWERL and begin measurement of meteorological variables and PM$_{10}$ concentrations from the established network stations from April to August 2020. These data provided insight into what happens when OHV activity suddenly stops prior to the annual windy period.

2. Methods

2.1. Surface emissivity measurements

Since 2013 PI-SWERL measurements of emissivity across the ODSVRA have been made on an annual basis in areas that allow as well as areas that restrict OHV activity. Measurements have been repeated each year, typically in the month of May, by revisiting locations that were established in 2013, which defined west to east and north to south transects (Fig. 1). Measurements have also been added in different years in, for example, areas where it was deemed critical to obtain data that could be used to define the change in emissivity as a function of distance past a riding-nonriding boundary.

Emissivity measurements were made using the PI-SWERL instrument following a standardized set of protocols that have been maintained from 2013 through to 2020. The PI-SWERL is shown in Fig. 2 on a sand surface at the ODSVRA. Briefly, the PI-SWERL consists of a cylindrical chamber (0.30 m diameter) that is open on one end. A test plate, with a central region that is open and equal in diameter to the inside of the PI-SWERL chamber and a thin metal lip that extends 0.04 m below the bottom, is inserted into the sand test surface. The test plate provides stability, ensures a consistent distance between the blade and the surface, and facilitates a seal between the PI-SWERL and the surface. The PI-SWERL is placed onto the test plate so that the open bottom of the PI-SWERL is aligned with the open section of the test plate.

Within the PI-SWERL, an annular blade is suspended from the top cylinder approximately 0.05 m above the test surface and connected to a motor at the top of the cylindrical chamber. When the motor spins the annular blade, a shearing stress (τ, N m^{-2}) is created on the test surface (Etyemezian et al., 2014) by its rotation. Clean air is injected into the cylinder at a flow rate of 100 L per minute (lpm), which mixes with the particle-laden air inside and is exhausted through a port on the top of the
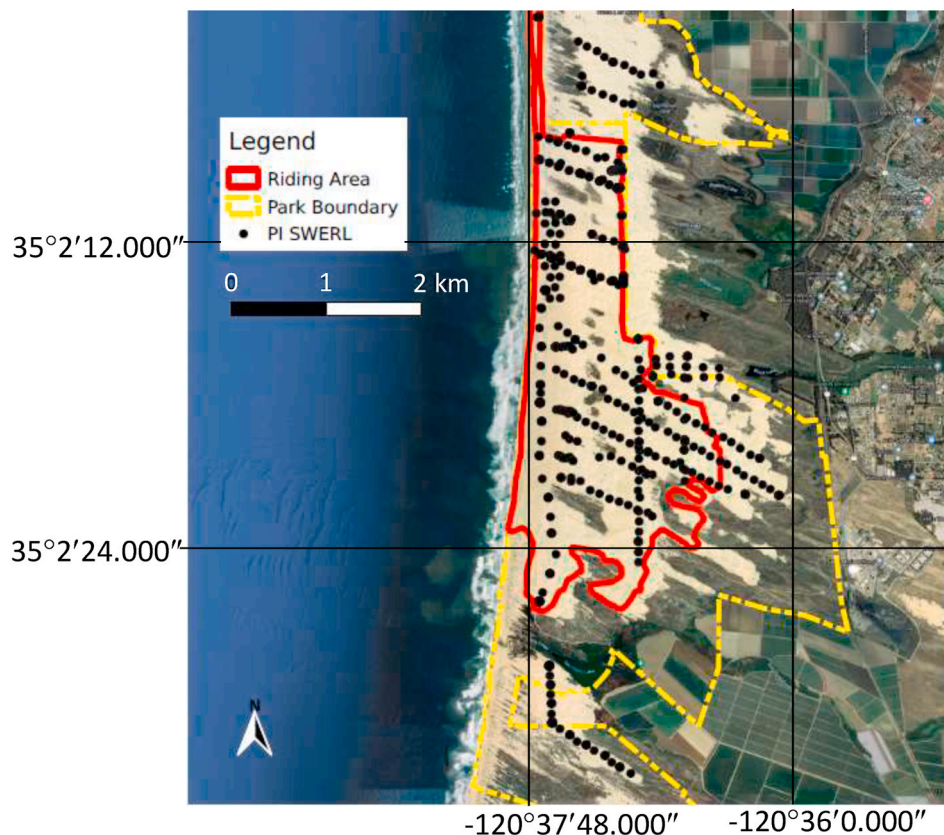

Fig. 1. The Oceano Dunes and the ODSVRA, central coast California, USA, and the locations of the PI-SWERL tests carried out between 2013 and 2020 identified with black circles.

Fig. 2. The PI-SWERL at a test location in the riding area of the ODSVRA.

chamber. Another small port at the top of the chamber is connected to a dust monitor (DustTrak 8520, TSI, Inc., Shoreview MN) and concentrations of suspended particles (mg m^{-3}) within the chamber are measured once per second. The dust monitor is equipped with a size cut inlet so that it measures PM$_{10}$.

For the testing carried out at the ODSVRA the PI-SWERL was operated with a set sequence of target RPM values (2000, 3000, and 3500, named the "Hybrid 3500" test). For the Hybrid 3500 test, 60 s of clean air flush are followed by a linear "ramping" increase of the blade rotation from 0 RPM to 2000 RPM over the course of 60 s. The rotation rate of 2000 RPM is held constant for 60 s corresponding to the first constant RPM "step", followed by a ramping increase to 3000 RPM over 60 s. The second step at 3000 RPM is held for 90 s, followed by a 60 s ramp to 3500 RPM, which is also held for 90 s. Following this, power to the motor is cut and the cylindrical chamber is flushed with clean air for 60 s. Coordination of motor speed, air flow control, and data collection and logging from the dust monitor and control components is automated.

Each RPM step corresponds to constant shear stress, τ, values (or $\tau = \rho_{air} u_*^2$ where u_* is shear velocity, m s^{-1} and ρ_{air} is air density, kg m^{-3}). The RPM is converted to a u_* value using the relationship from Etyemezian et al. (2014):

$$u_* = C_1 \alpha^4 RPM^{C2/\alpha}. \tag{1}$$

where C_1 is a constant (0.000683), C_2 is a constant (0.832), and α, which has a value between 0.8 and 1 that varies with the surface roughness, and which was assumed equal to unity based on the surface roughness designation of smooth sand.

Dust emissions at each of the three steps where RPM is held constant are calculated by averaging the 1 s dust concentrations over the duration of the step and using:

$$E_i = \frac{\left(C_{DT,\,i} \times \frac{F_i}{60 \times 1000}\right)}{A_{eff}}. \tag{2}$$

where E_i is the PM$_{10}$ dust emissions in units of mg m^{-2} s^{-1} at the ith step, CDT,i is the average DustTrak PM$_{10}$ in mg m^{-3}, F_i is the clean air flow rate (m^3 s^{-1}) in (and out of) the PI-SWERL chamber, and A_{eff} is the effective area of the PI-SWERL annular blade (0.035 m^2 as recommended by Etyemezian et al., 2014).

From 2013 through to 2019, all or a portion of the measurement grid was revisited annually with the measurements typically completed in five days, weather permitting. The details of the sampling procedure through this time are provided in Mejia et al. (2019). Each PI-SWERL Hybrid 3500 test results in three paired values of E and u_*, not all of

which may pass a quality control screening. A total of 2797 valid measurements of emissivity were available from riding areas and 1113 from non-riding areas between 2013 and 2019.

In 2020, upon notice that the ODSVRA had eliminated access to OHV activity for the public, two PI-SWERL measurement plans were executed. Thirty measurement locations (Fig. 3) that represent a sub-set of the sampling grid shown in Fig. 1 were selected in the area known as the Lagrande Tract, where camping has traditionally been focused and where the emissivity has been observed to be higher compared to the rest of the active OHV areas. These sites were visited on a weekly basis, weather permitting, and emissivity characterized with PI-SWERL using the Hybrid 3500 test cycle. Testing was carried out between 11:00 and 17:00 h local time if precipitation or fog conditions had not occurred over the three preceding days. During the 2020 study period, 186 Hybrid 3500 PI-SWERL tests were made in the Lagrande Tract.

To ensure a representative sample of emissivity across the ODSVRA in 2020 to allow comparison with the full grid measured in 2019, a subset of the measurement positions drawn from the entire sampling grid shown in Fig. 1, were selected for measurement (Fig. 3). A bootstrapping resampling procedure was used on the 2019 sample locations to determine the number of samples in the sub-set that would keep the transect end points the same in 2020, preserve the spatial coverage, and return to points on the 2019 grid. The re-sampling procedure suggested that 100 samples would yield a mean emissivity value within 0.12 mg m^{-2} s^{-1} of the true population mean, with 50% probability of falling within approximately 0.06 mg m^{-2} s^{-1}. Unfortunately, due to constraints imposed by weather and time in May 2020, testing was completed at only 60 locations and none were in the non-OHV activity areas.

Extensive quality control was conducted to ensure the integrity of the data collected with the PI SWERL. Collocations were conducted at the beginning, end, and every ten measurements, wherein both PI SWERL units were used in close proximity for three measurements. This allows field operators to diagnose problems in-situ and provides traceable measurements that can be used to quantify discrepancies between the two instruments. Prior to averaging each of the three constant RPM Levels (2000, 3000, 3500), a median filter of radius five was run over the time series to remove noise from the PM$_{10}$ sensor. For each measurement taken, visual quality control was conducted to flag any RPM levels with significant PM$_{10}$ sensor or RPM sensor malfunction. This approach allows for RPM set points in the Hybrid 3500 with flags to be removed in later analyses and serves as a check on values where the median filter may not have been sufficient to remove noise.

2.2. Meteorological and PM measurements across the ODSVRA

Between 2017 and 2020, a meteorological and airborne dust monitoring network, consisting of between seven and 11 monitoring locations was operated at the ODSVRA in active riding areas, at two locations near the eastern border of the Park downwind of the sand dune complex, and two locations east of the ODSVRA's eastern border on land owned by the Philips 66 Petroleum Company and at a California Department of Forestry and Fire Protection (CDF) station (Fig. 4). The CDF station also hosts instruments operated by the San Luis Obispo County Air Pollution Control District to measure regional PM (PM$_{10}$ and PM$_{2.5}$) concentrations. These monitoring stations serve to characterize wind conditions and the distribution of airborne particulate matter (PM) during high wind events that contribute to high concentrations of PM$_{10}$ across the spatial domain of the ODSVRA, and beyond. The position of a monitoring location once established has remained constant from 2017 through 2020.

A measurement station is shown in Fig. 5. In 2019 and 2020 wind speed and direction were measured using 2-D sonic anemometry (Met-SENS500, Campbell Sci., Logan UT). This instrument also provides measurement of ambient temperature, relative humidity (RH) and barometric pressure. In 2017 and 2018 wind speed and direction were
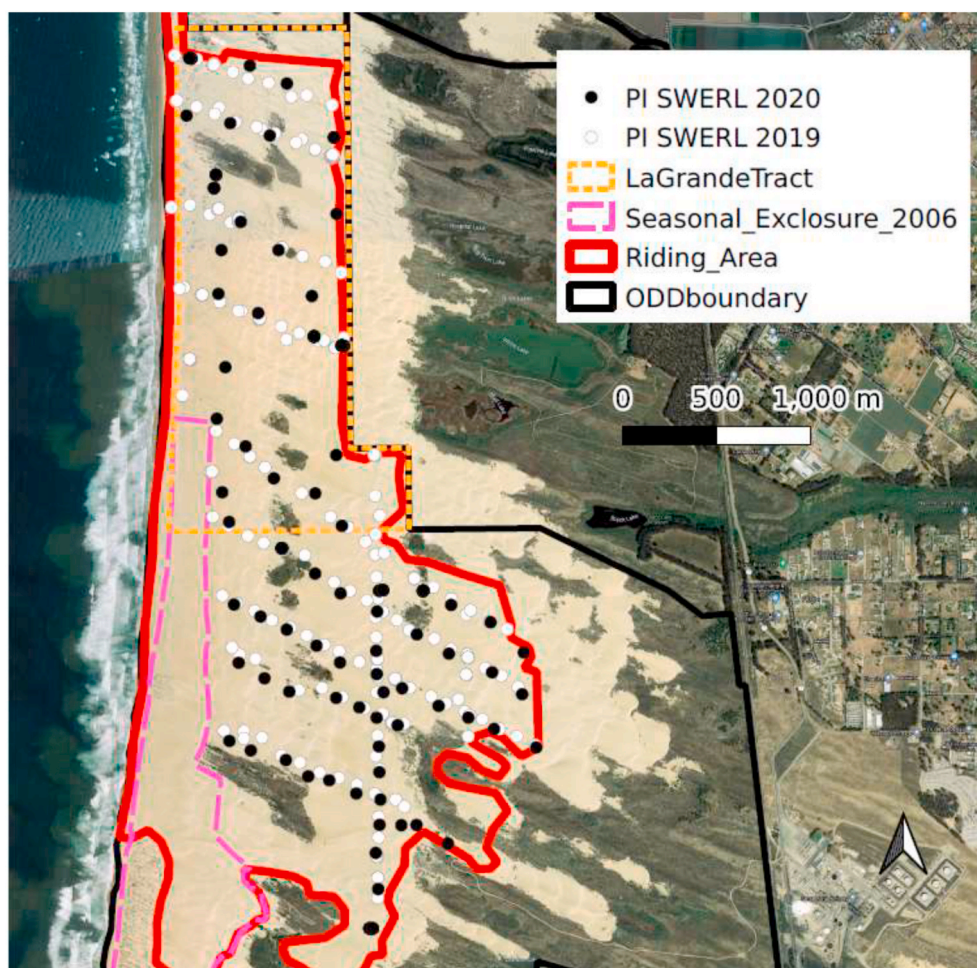
Fig. 3. Locations of PI-SWERL tests in the Lagrange Tract (defined by yellow border) and across the established measurement grid in 2019 (white circles) and in 2020 (black circles). (For interpretation of the references to colour in this figure legend, the reader is referred to the Web version of this article.)

measured using a propellor type anemometer and wind vane combination (Model 05103, RM Young, Traverse City, MI). The wind sensing and PM instruments were positioned 3.5 m AGL for the stations within the area of the ODSVRA with OHV activity. Particulate matter at each station was measured using an instrument that measures particle counts in eight size bins per sampled flow volume (212-2 Particle Profiler, MetOne Instruments, Grants Pass, OR) using an optically-based measurement instrument. These particle count bins are used to derive a PM_{10} concentration on a minute and hourly basis.

To achieve a measure of PM_{10} from this instrument that can be compared between stations and to the PM_{10} measured by an EPA Federal Equivalent Method a calibration procedure was developed to convert the particle count data to an equivalent mass based PM_{10} concentration. Cross-calibration of each 212-2 instrument with a Beta Attenuation Monitor (BAM-1022, MetOne Instruments, Grants Pass, OR) was achieved by collocating them in an environmentally controlled chamber and establishing a unit-specific calibration relation. The instruments are rack-mounted in the chamber beside the BAM and a filter-based sampler (cyclone-style sampler). Under controlled temperature and humidity conditions dust is created by operating the PI-SWERL instrument at a constant above threshold u_* on a bed of Oceano Dune sand to simulate saltation and mixed thoroughly within the chamber exposing all instruments to the same PM_{10} concentrations. The data stream (particle counts in each bin size per unit time) from the 212-2 units and the BAM ($\mu g \ m^{-3}$) are recorded by a datalogger.

Each 212-2 outputs a data string corresponding to the counts of particles that are greater than a given diameter in a given volume. In order to translate this into a mass-equivalent concentration: 1) the number of particles in a size bin is calculated by subtracting the number of counts associated with all larger size bins, 2) a diameter representing all the particles within a size bin is estimated (taken to be the geometric mean of the minimum and maximum of the size bin), 3) the volume of an individual particle of the characteristic diameter of the size bin is calculated assuming particles are spheres, 4) the total volume of particles in a volume of air is calculated by multiplying the volume of a single particle by the number of particles in the size bin in the known volume of air, and 5) a particle density of 2600 kg m^{-3} is used to estimate the mass concentration of particles in the size bin. The cumulative mass concentration of particles through size bin 6 is denoted as PMbin6. A calibration relationship between the BAM and the PMbin6 value is defined through the paired values of BAM-measured PM_{10} and calculated PMbin6 for each 212-2 instrument. An example of this relation is shown in Fig. 6. The consistency of the calibration relations among the 212-2 units was good. The mean slope value for all units combined was 0.238 (± 0.063) and mean intercept was 4.704 (± 0.869). The mean correlation coefficient was 0.950 (± 0.013).

In addition to the chamber testing, an in-Park calibration station was established in 2020. This station consisted of a BAM, mounting hardware for two 212-2 units, wind speed, wind direction and RH instruments, and datalogging with modem telemetry. The purpose of the in-Park calibration was to determine the performance of the 212-2 and BAM instruments under ambient conditions at the ODSVRA. Of concern was their ability to perform under high wind conditions and whether this resulted in a bias in the measurement compared to the
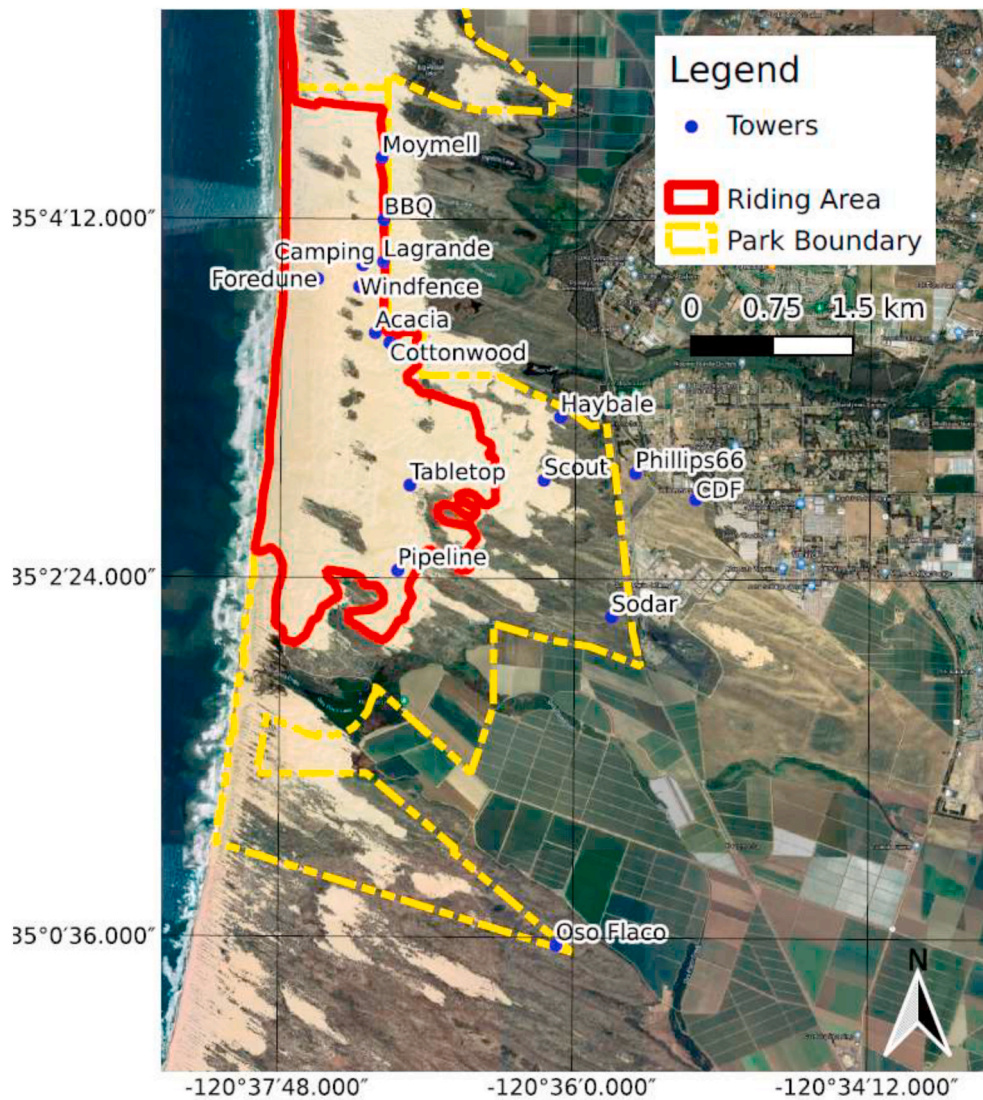
Fig. 4. Locations of the meteorological and airborne dust monitoring stations within and exterior to the ODSVRA. Haybale, Phillips 66, CDF, SODAR, and Oso Flaco are downwind of active emission areas.

BAM. In 2020, 10 of the 212-2 units were collocated with the in-Park BAM.

The available data from the in-Park calibration testing indicated that the 212-2 units were not adversely affected by wind speeds that exceeded 5 m s^{-1} compared to the chamber conditions (i.e., no wind). The mean slope value and intercept values were 0.224 ($\pm$0.042) and 5.096 ($\pm$3.437), respectively. The mean correlation coefficient was 0.917 ($\pm$0.119). The differences in slope, intercept, and correlation coefficient are due to the dynamic nature of the field environment, but the degree of change indicates that under these conditions the correlation between the two instruments remained high and provides confidence that the 212-2 performs well at the ODSVRA. Because we do not have in-Park calibrations for all relevant stations, the PMbin6 data were converted to PM$_{10}$ using the March 2020 chamber-derived relationships for each 212-2 unit. Using the 212-2 chamber-derived calibration coefficients ensures the inter-comparisons among the different units can be made with confidence, as differences in 212-PM$_{10}$ measurements are not due to a mixing of calibration methods, i.e., in-lab versus in-Park.

Wind power density (WPD, W m^{-2}) is an effective quantity for evaluating the relation between the energy in the wind and the response of the dust emission system of the ODSVRA. Wind power density (WPD) is defined as (e.g., Kalmikov, 2017):

$$\mathrm{WPD} = 0.5\,\rho_a u^3. \tag{3}$$

where ρ_a is air density (kg m^{-3}), and u (m s^{-1}) is wind speed (at a known height). WPD is a quantitative measure of wind energy related to sediment transport by wind (Bagnold, 1941; Chepil, 1945; Skidmore, 1998) and is used to parameterize erosive wind power in the United States Department of Agriculture's, Wind Erosion Prediction System (Hagen et al., 1999). WPD is calculated for each hour of mean wind speed at all the monitoring stations.

3. Results

3.1. PI-SWERL emissivity data 2013–2019

The distribution of emissivity (E, mg m^{-2} s^{-1}) as a function of the three shear velocity (u_*, m s^{-1}) settings of the Hybrid 3500 test cycle of the PI-SWERL for the riding and non-riding areas of the ODSVRA amalgamated from 2013 to 2019 are shown in Figs. 7 and 8, respectively. For all the u_* set-points (i.e., u_* values corresponding to the three constant RPM values, 2000, 3000, 3500) the distribution of E for the seven years of data are positively skewed (Figs. 7 and 8). As these data are skewed with a tail of high emissivity values, a single factor Analysis
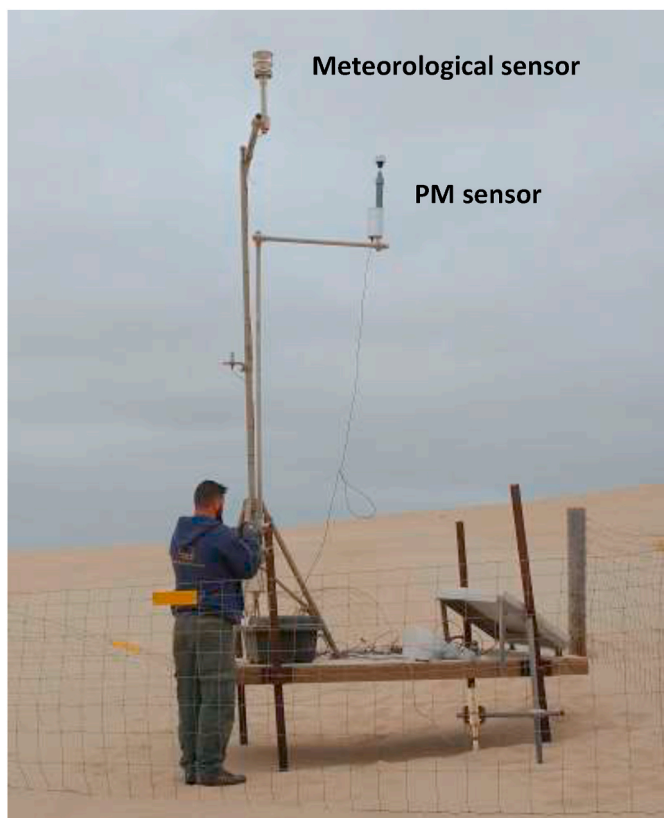
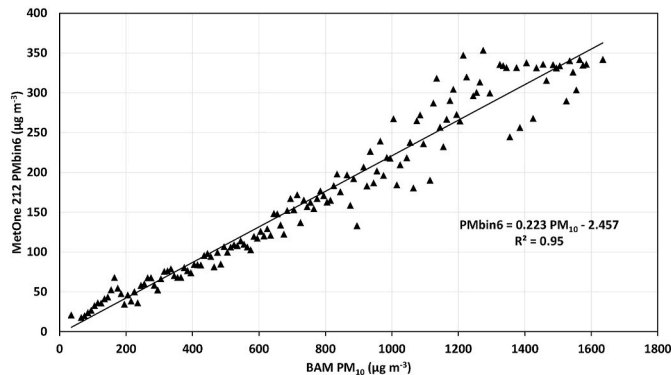**Fig. 5.** A meteorological and PM monitoring station within the ODSVRA.

Fig. 6. An example of the calibration relationship between BAM and PMbin6 from chamber testing for the MetOne 212 instrument deployed at the BBQ site (Fig. 4).

Fig. 7. The distribution of emissivity (E, mg m^{-2} s^{-1}) as a function of the three shear velocity (u_*, m s^{-1}) settings for the riding areas of the ODSVRA amalgamated from 2013 to 2019.

of Variance (ANOVA) was used to determine if the distribution of E values for the same u_* were significantly different between the riding and non-riding areas. The results of these ANOVA tests are shown in Table 1. For each emissivity data pair for the same set-point u_* the non-riding area emissivity is statistically different from the riding area. This is based on the P values being less than 0.05 and the F values being greater than the F critical values.

Emissivity scales as a power function of u_* and the relation for the riding and non-riding area E data for 2013–2019 are shown in Fig. 9. These data represent the mean E at each of the u_* set points with the error bars representing the standard error of the estimate (i.e., standard deviation of the mean/((# observations-1)$^{0.5}$). The riding area, according to the PI-SWERL data has greater emissivity than the non-riding area for equivalent values of u_*. We recognize that establishing the emissivity relations based on three shear velocity (u_*, m s^{-1}) settings is a
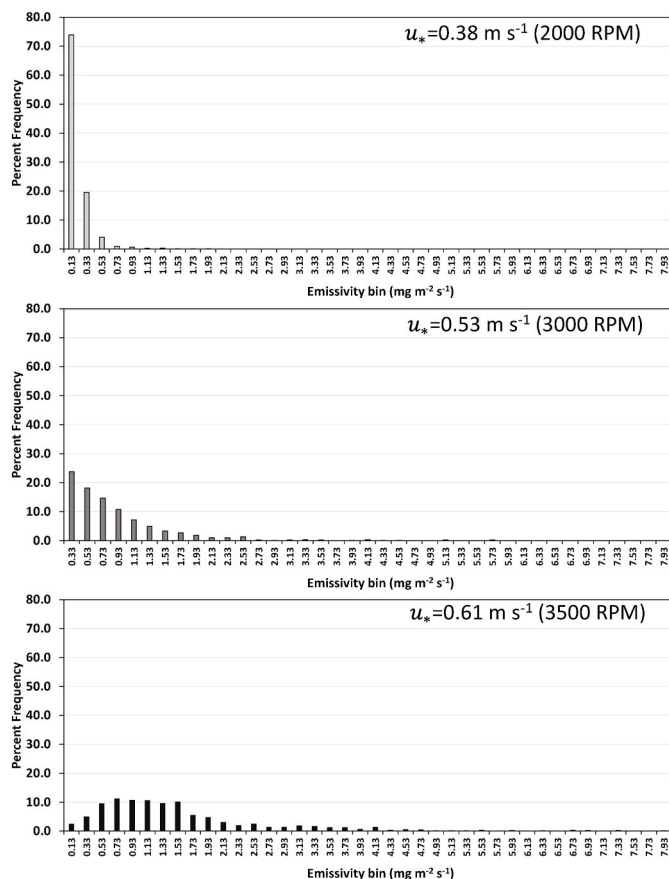
limitation of the methodology, but this was necessitated by the need to complete the measurements in a limited amount of time each year. For each set-point there are, however, hundreds of data points that are used to calculate a mean value.

The mean emissivity relations for riding and non-riding areas can be disaggregated to examine for geographic influence on the emissivity across space. The emissivity data for the non-riding areas were grouped as: northern dune preserve, areas east of the riding/non-riding boundary in the middle zone of the ODSVRA, and the southern dune preserve (Fig. 10). For each of the three zones an ANOVA test was done on the paired data for each set-point u_*. The ANOVA tests indicated that the mean emissivity values for each test u_* are significantly different between the geographic locations at the P = 0.05 level, with the north having higher emissivity than the east and the south, and east higher than the south (Fig. 10).

The gradient of increasing emissivity towards the north in the non-riding area is also observed in the emissivity data for the riding area of the ODSVRA. This is demonstrated in Fig. 11, which shows the increase in mean emissivity as a function of latitude bins of 0.005 (decimal) degrees expressed as the increase in emissions when normalized to the southern-most measurement group for all available data (i.e., mean emissivity in latitude bin/mean emissivity in southern-most latitude bin) from 2013 to 2019. This holds for each of the three test u_* values (Fig. 11). In each latitude bin for each test u_*, the emissivity represents the mean of all tests that fall within the bin.

As noted previously, the non-riding area PI-SWERL data (Fig. 10) indicate a north-south gradient of emissivity. Comparing emissivity between the riding and non-riding areas along a north-south gradient cannot be accomplished using a single increment of decimal degrees of
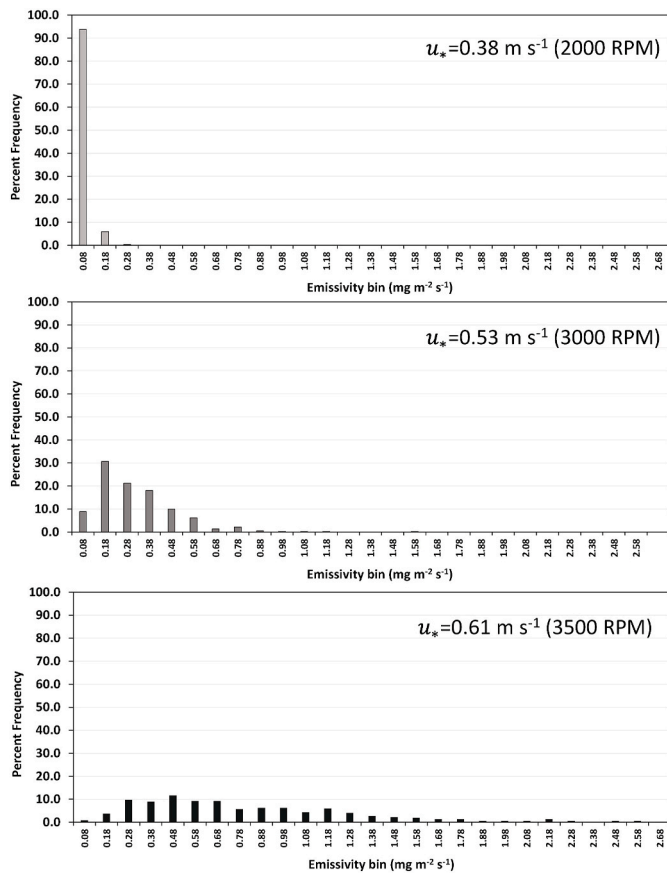
Fig. 8. The distribution of emissivity (E, mg m^{-2} s^{-1}) as a function of the three shear velocity (u_*, m s^{-1}) settings for the non-riding areas of the ODSVRA amalgamated from 2013 to 2019.

latitude as the tests in the riding areas of the north and the south extend outside the latitude range of the riding area tests. To provide some indication of the difference between riding and non-riding emissivity north to south, the data are grouped into six latitudinal bins that pair the north and south non-riding area tests with a portion of the south and north riding area tests, respectively. Where there is latitudinal overlap among the riding and non-riding tests, they are grouped in bins of 0.01 decimal degrees. The mean riding area emissivity normalized to the mean non-riding area in each latitudinal bin and for each u_* set point is shown in Fig. 12. In all cases, riding emissivity is greater than non-riding emissivity with the variability decreasing with increasing u_*. For the u_* set points of 0.53 and 0.61 m s^{-1} the ratio is approximately a factor of three for $u_* = 0.53$ and a factor of two for $u_* = 0.61$ with no strong signature of change as a function of latitude.

3.2. PI-SWERL emissivity data 2013–2019 versus 2020 sub-sample

As identified earlier, a sub-set of the established PI-SWERL larger sampling grid was measured in 2020. Unfortunately, it was not possible to measure all the 100 selected test locations resulting in exclusion of the non-riding areas. The distributions of E for the three u_* set points of Hybrid 3500 test cycle for the 2020 sampling in the riding area are shown in Fig. 13. These also exhibit skewed distributions as was observed for the 2013–2019 data for riding and non-riding areas. A single factor ANOVA test between the paired data for each set point u_* between 2019 and 2020 was carried out (Table 2). For these tests there is no significant difference in E for the $u_* = 0.38$ m s^{-1} (RPM = 2000) set points, but significant differences between the E values for the two higher u_* set-points.

The mean emissivity relations as a function of u_* for the 2020 and 2019 PI-SWERL measurements are shown in Fig. 14, with both measurement campaigns taking place in the month of May. The data points represent the mean E at each of the u_* set points with the error bars representing the standard error of the estimate (i.e., standard deviation
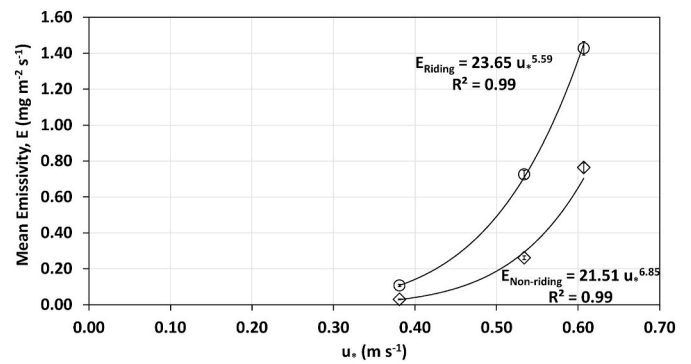

Fig. 9. The relation between mean E (mg m^{-2} s^{-1}) and u_* (m s^{-1}) for the amalgamated data from 2013 to 2019 for the riding (circles) and non-riding areas (diamonds). Error bars represent the standard error of the estimate (standard deviation/(#observations-1)$^{0.5}$).
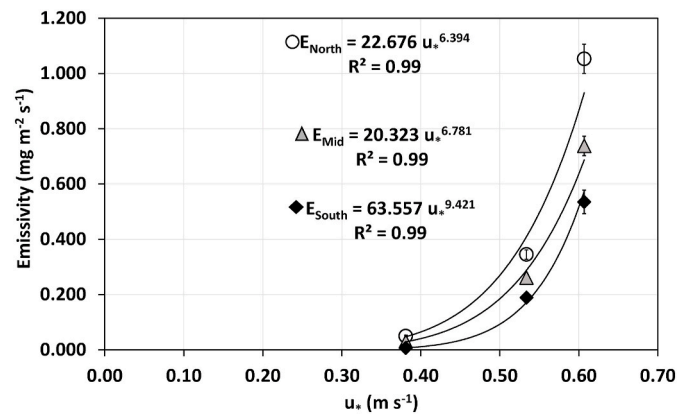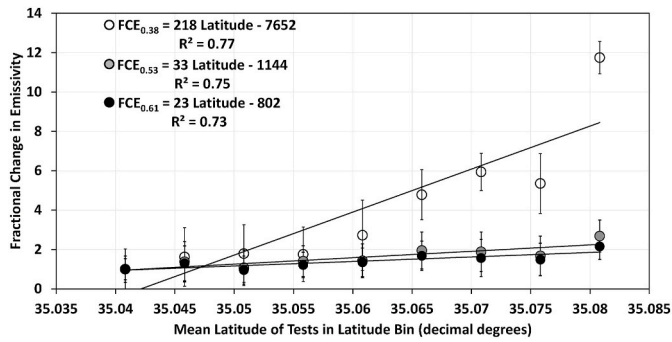

Fig. 10. The relation between mean E (mg m^{-2} s^{-1}) and u_* (m s^{-1}) compared by geographic position for the non-riding areas: white circle, north; grey triangle, middle, black diamond, south. Error bars represent the standard error of the estimate (standard deviation/(#observations-1)$^{0.5}$).

Table 1
ANOVA results comparing non-riding area emissivity distribution to riding area emissivity for data from 2013 to 2019.

Groups	u_* (m s^{-1})	Count	Sum E (mg m^{-2} s^{-1})	Mean E (mg m^{-2} s^{-1})	Variance	F	P-value	F crit
Non-Riding	0.38	372	11.158	0.030	0.001	75.299	1.2E-17	3.849
Riding	0.38	934	99.636	0.107	0.029			
Non-Riding	0.53	372	97.366	0.262	0.035	159.417	1.5E-34	3.849
Riding	0.53	934	677.750	0.726	0.488			
Non-Riding	0.61	369	97.366	0.262	0.035	114.573	1.1E-25	3.849
Riding	0.61	929	1326.372	1.428	1.321			

Fig. 11. The fractional increase in emissivity as a function of position along the north (35.08 decimal degrees) to south (35.04 decimal degrees) gradient of the PI-SWERL tests in the ODSVRA riding area (2013–2019). Data represent mean emissivity in each latitudinal bin normalized to the mean emissivity in the southern-most latitude bin for the three PI-SWERL u_* set-points: 0.38 m s^{-1}, 0.53 m s^{-1}, and 0.61 m s^{-1}. Error bars represent the coefficient of variation (standard deviation/mean).

of the mean/(# observations-1)$^{0.5}$). The ANOVA tests indicated that the E values at each set point were statistically different. Fig. 14 suggests that in May 2020 emissions of PM$_{10}$ were lower than in May 2019 in the same representative area of the ODSVRA (Fig. 3).

3.3. PI-SWERL emissivity data, Lagrande Tract 2020 repeated survey

PI-SWERL tests were repeated within the Lagrande Tract area from April to October 2020 during which time OHV activity was largely prohibited (NB, no measurements were made in August). The locations of the tests remained constant during that time (Fig. 3). It must be recognized that although the positions of the tests remained the same, the sand was intermittently being transported by the wind.

The wind redistributes the sand and the bedforms (ripples and dunes) migrate in the direction of the sand transporting wind during transport events. Although the tests were conducted at the same locations, clearly

the sand at those locations was likely not the same sand from the previous tests. The wind essentially randomizes the surface with each transport event and makes comparison of emissivity at a particular position questionable. For these data it is more reasonable to aggregate them by creating a mean emissivity for the tests made during set periods of time, for example, by month.

A comparison is made of the mean normalized emissivity as a function of month in Fig. 15 for: 1) the 2013–2019 mean riding area emissivity, 2) 2019 mean emissivity for the same test locations (Lagrande Tract), and 3) the 2013–2019 mean non-riding area emissivity. In each case the mean monthly values are divided by the mean monthly emissivity for the Lagrande Tract in 2020. For the 2013–2019 and the 2019 mean Lagrande Tract normalizations, on a monthly basis, the 2020 Lagrande Tract emissivity is lower for both comparisons by a factor range of 0.43–0.74. Compared with the non-riding area normalization the Lagrande Tract mean emissivity by month is greater than the non-riding mean emissivity by a factor range of 1.1–1.6.

3.4. PM concentration and wind data from the in-Park monitors, 2017–2020

The meteorological and PM monitoring stations provide data to evaluate the relation between wind and PM$_{10}$ concentrations across the domain of the ODSVRA and at key points downwind (e.g., Phillips 66, SODAR, and CDF sites) and through time. To quantify WPD at each monitoring location the hourly mean values are summed for the hours identified where the PM$_{10}$ (MetOne 212-BAM corrected, using chamber-based calibration relationships) concentrations are paired with the station-measured wind speed. To define the relation between monthly TPM$_{10}$ and TWPD for the in-Park stations in 2020, we calculated mean hourly PM$_{10}$ and mean hourly wind speed measured at 3.5 m AGL for each in-Park monitoring station.

To set the threshold of WPD for the summation calculation we first examined the relation between average PM$_{10}$ and mean binned wind speed for monitoring stations spanning the north-south dimension of the in-Park network (Moymell, Cottonwood, and Pipeline) in 2020 (Fig. 16). This figure shows that the local concentration of PM$_{10}$ begins to increase
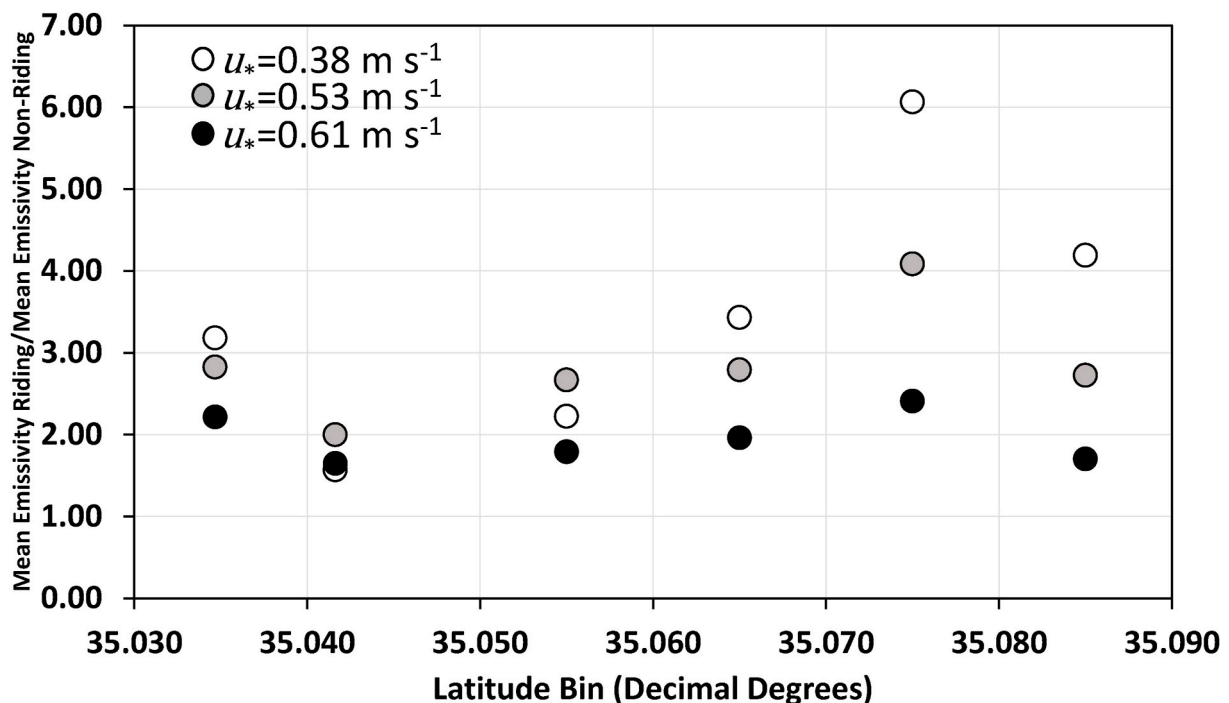
Fig. 12. Mean emissivity in riding area normalized by mean emissivity of non-riding areas as a function of 0.01 decimal degree latitude bins. Color represents PI-SWERL u_* set points: white, 0.38 m s^{-1}; grey 0.53 m s^{-1}; black, 0.61 m s^{-1}.

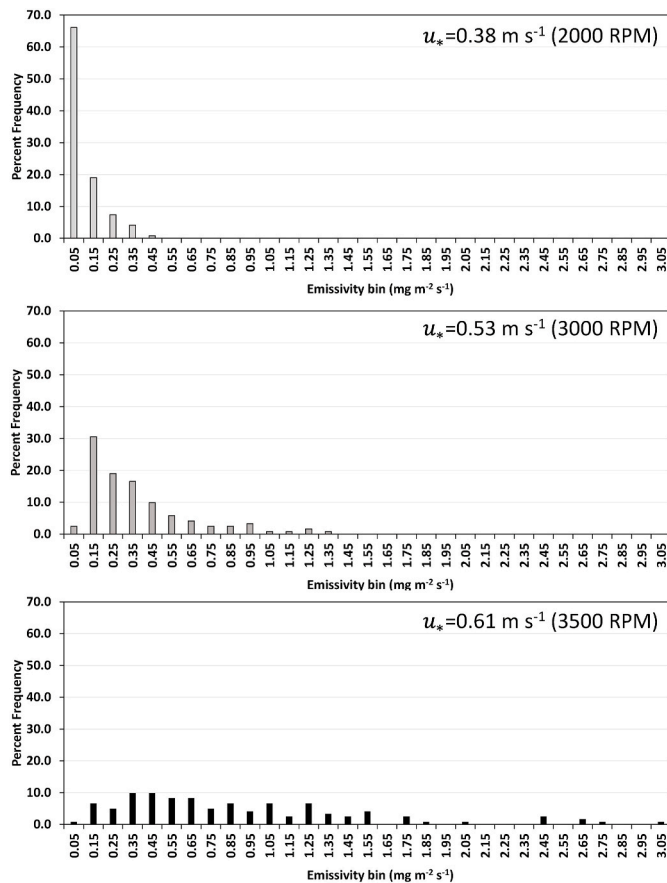**Fig. 13.** Frequency distributions of E (mg m^{-2} s^{-1}) for PI-SWERL tests made in the riding area in 2020.

when the 3.5 m AGL wind speed reaches and then exceeds 5 m s^{-1}, which was typical for most stations. We use 5 m s^{-1} mean hourly wind speed to set the lower limit for WPD (77 W m^{-2}) for the summations of total WPD (TWPD, W m^{-2}) and total PM$_{10}$ (TPM$_{10}$, µg m^{-3}) for each month. As the in-Park stations are surrounded by sand that can be mobilized by the wind, no wind direction filter was applied.

Examples of relations between TPM$_{10}$ and TWPD for four sites that span the north-south dimension of the monitoring network are shown in Fig. 17 for 2019 and 2020 (for the same 4 stations). For all other in-Park stations, in all years for which monthly data are available (2017–2020), a linear relation between TPM$_{10}$ and TWPD also holds.

The ratio of TPM$_{10}$:TWPD (µg W^{-1} m^{-1}) serves as a metric to evaluate how the dust emission system is changed by changes to or in the landscape. With no changes to the surface where the emissions originate from, this ratio will reflect the efficiency of the wind and saltation system to produce PM$_{10}$ for the prevailing environmental conditions during the period of interest and should remain stable if the environmental conditions remain stable. If, however, the surface from which the emissions are originating from is changing, for example, by removal of the PM$_{10}$ source material or coarsening of the surface sand (i.e.,

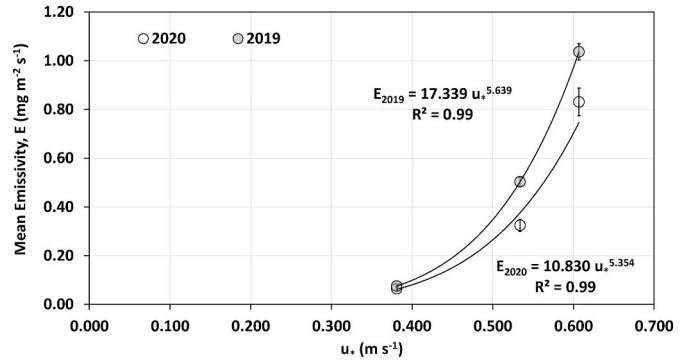**Fig. 14.** The relation between mean E (mg m^{-2} s^{-1}) and u_* (m s^{-1}) for the riding area in 2019 (grey circles) and 2020 (white circles). Error bars represent the standard error of the estimate (standard deviation/(#observations-1)$^{0.5}$).
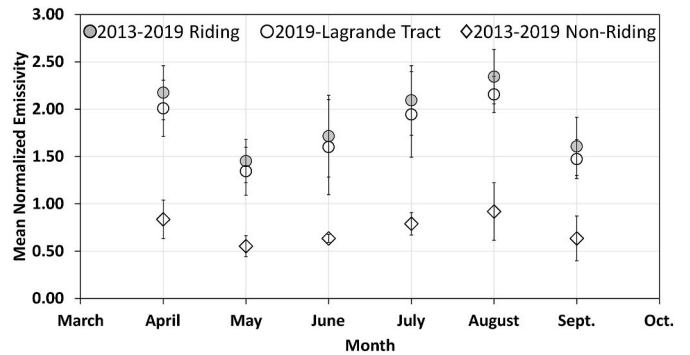

Fig. 15. The mean normalized emissivity of the three u_* set-points as a function of month for: 1) 2013–2019 mean riding area emissivity (grey circles), 2) 2019 Lagrande Tract mean emissivity (white circles), and 3) 2013–2019 mean non-riding riding area emissivity (diamonds). Normalization is by division with the 2020 Lagrande Tract mean emissivity for each, by month. Error bars represent the standard deviation of the mean normalized emissivity.
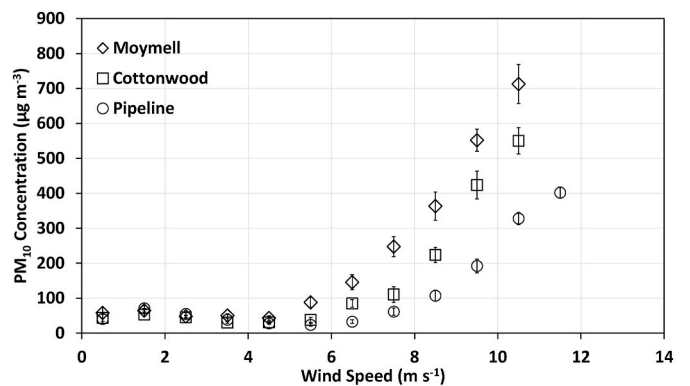

Fig. 16. The relation between mean PM$_{10}$ concentration (µg m^{-3}) and wind speed for three in-Park stations in 2020. Error bars represent the standard error of the estimate (standard dev/(#observations-1)$^{0.5}$.

Table 2
ANOVA results comparing riding area emissivity between 2019 and 2020.

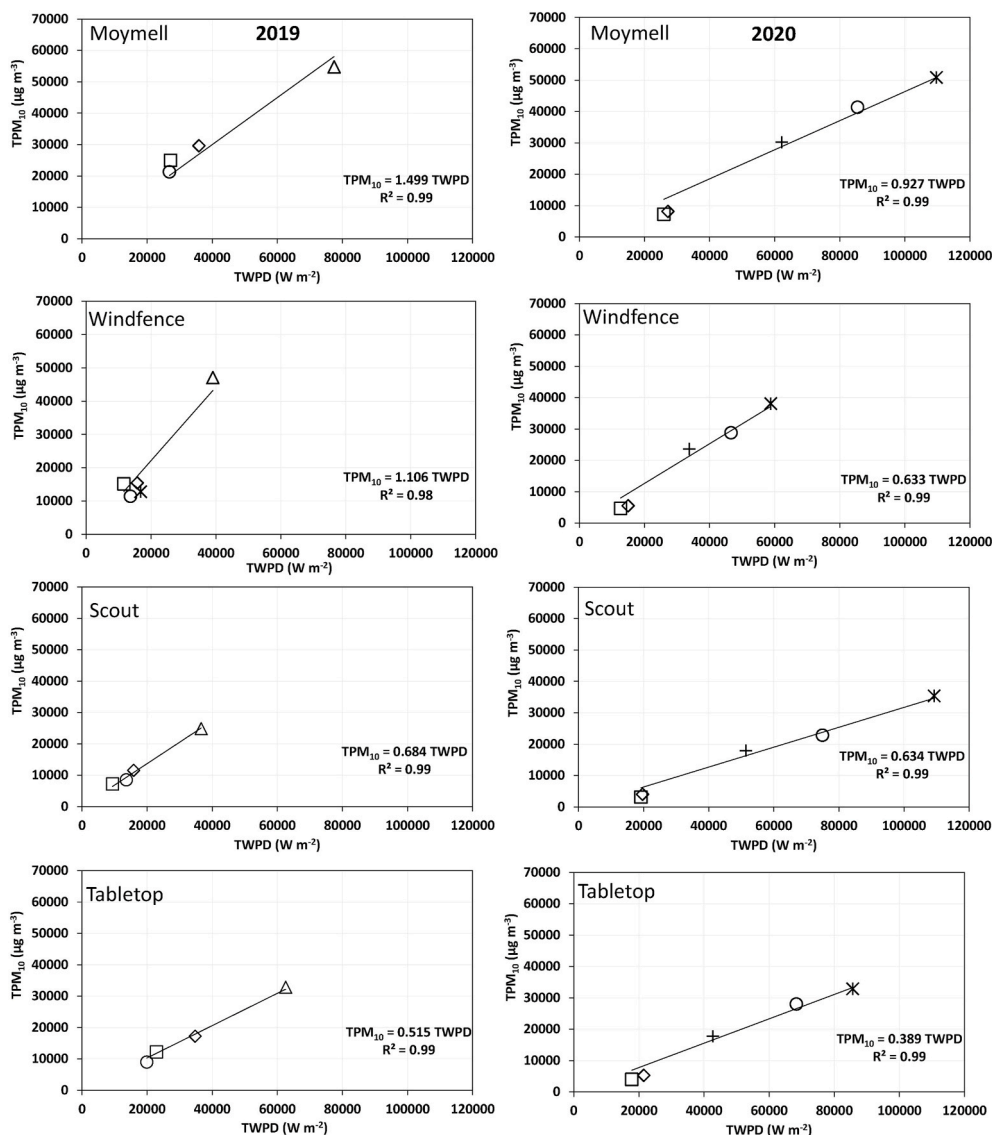| Groups	u_* (m s^{-1})	Count	Sum E (mg m^{-2} s^{-1})	Mean E (mg m^{-2} s^{-1})	Variance	F	P-value	F crit
Riding 2020	0.38	118	7.590	0.064	0.007	1.373	0.242	3.865
Riding 2019	0.38	285	21.399	0.075	0.007			
Riding 2020	0.53	122	39.586	0.324	0.076	31.921	3.035E-08	3.865
Riding 2019	0.53	284	142.927	0.503	0.090			
Riding 2020	0.61	122	101.389	0.831	0.388	10.704	0.001	3.865
Riding 2019	0.61	282	292.438	1.037	0.316			

Fig. 17. Examples of the relation between TPM_{10} and TWPD for stations Moymell, Windfence, Scout, and Tabletop for 2019 (left) and 2020 (right). Shape indicates the month: +, April; □, May; x̂, June; ◇, July; □, August; △, September.

increasing mean grain diameter), the ratio should diminish as dust production by saltation processes becomes less efficient in producing PM_{10} dust. There is a limit to the explanatory power of this ratio, which is that if winds are at, or close to, the designated threshold speed either at the monitoring location or in the source area for a large part of the record, the value becomes unstable due to a potential paucity of data but also because as wind speed diminishes the strength of the coupling between the wind and the saltation-generated PM_{10} weakens and is subject to influence of PM_{10} from other sources.

To demonstrate how the TPM_{10}:TWPD ratio changed through time in 2019 and 2020, the ratio as a function of month is presented in Fig. 18 for the same four stations. The change, by month, in the TPM_{10}:TWPD ratio for the 2019 data (Fig. 18) was not consistent across all in-Park stations, most in-Park stations (7 of 8) showed an increase to a maximum followed by a decline to a lower value in the last month of observation. One station, however (Pipeline, not shown), showed a linear increase with increasing time for the five month-long record. For the 2020 data, the change in the TPM_{10}:TWPD ratio as a function of month for the same four stations are also shown in Fig. 18. The change, by month, in the TPM_{10}:TWPD ratio for the 2020 data was consistent across all in-Park (11 stations) and out-of-Park stations (4 stations) and

showed a linear decrease in the value of the ratio with increasing time.

The change of the TPM_{10}:TWPD ratio as a function of time for all available in-Park stations in 2019 and 2020 is shown in Fig. 19. The TPM_{10}:TWPD ratio in this figure is normalized to the value in the first month of observation (i.e., mean monthly ratio [all stations] in month n/ mean monthly ratio [all stations] in first month of observation). In 2019, the mean ratio value for all stations combined increases by ≈11.6% for each subsequent month of observation (Fig. 19). For the out-of-Park stations (CDF, Philips 66, Sodar and Strawbale), there is also an increase in the normalized ratio value of similar magnitude from the first month (June) to the maximum value in August, with a monthly increase of ≈15.2% (Fig. 19). A similar temporal pattern is also observed for the mean normalized TPM_{10}:TWPD ratio for all in-Park stations for the available record of May through September for 2017 and 2018 (Fig. 20).

The mean normalized TPM_{10}:TWPD ratio for the in-Park stations in 2020 (Fig. 19), shows that the mean ratio value decreased by ≈11.6% for each month of observation inside the Park and by 15.6% for stations outside the Park. The out-of-Park stations measure PM_{10} that has been dispersed by the ambient winds and are not subject to direct local emissions of particulate matter.
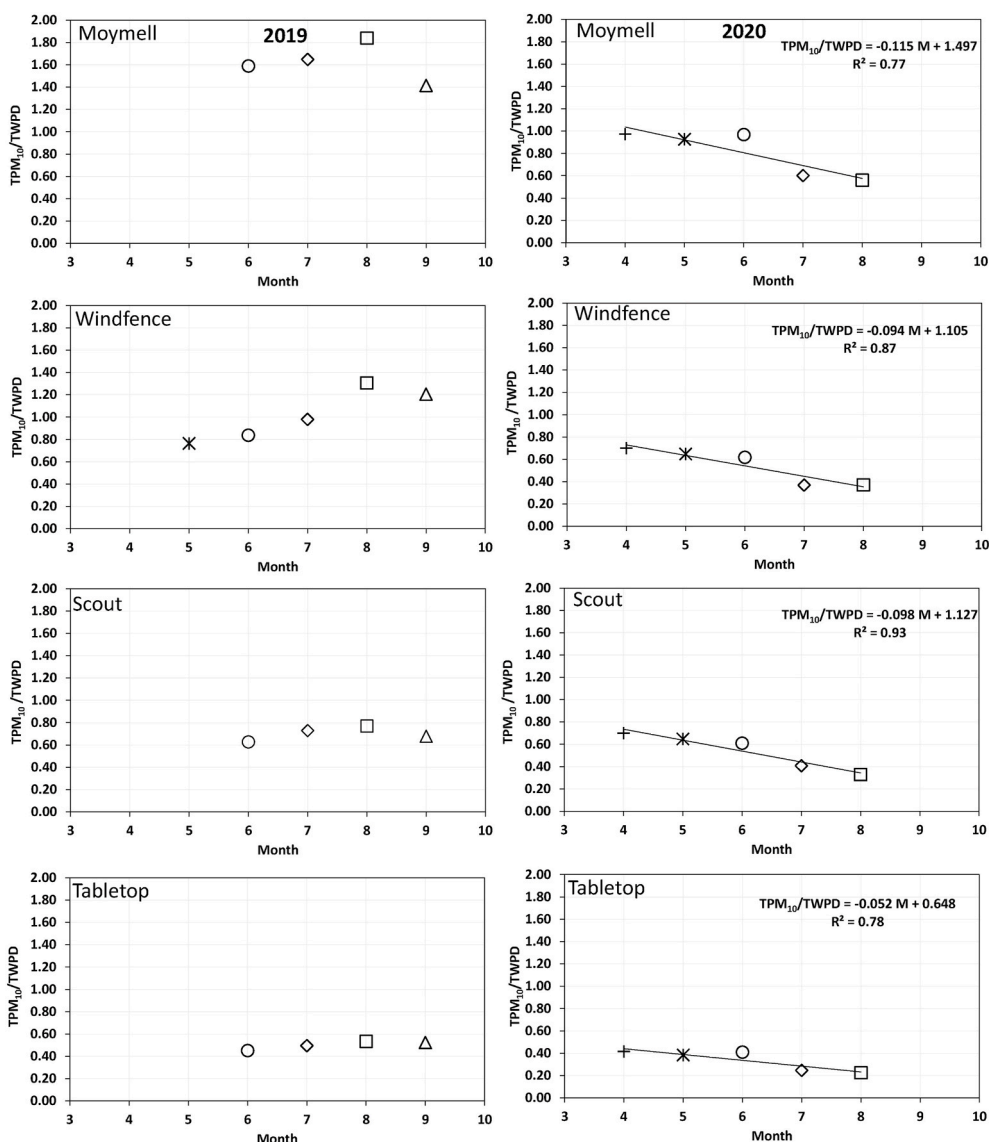
Fig. 18. The TPM$_{10}$:TWPD ratio for stations Moymell, Windfence, Scout, and Tabletop for 2019 (left) and 2020 (right). Shape indicates the month: +, April; □, May; x̂, June; ◇, July; □, August; △, September.

3.5. PM$_{10}$ and wind conditions, Oso Flaco monitoring site

Hourly data of PM$_{10}$ (measured at 3 m AGL) and wind speed (measured at 10 m AGL) were used to calculate TPM$_{10}$ and TWPD for winds between 225° and 326° and at speeds >7.5 m s^{-1} for the Oso Flaco station for 2019 and 2020, for the months April to September. The Oso Flaco station PM$_{10}$ was observed to generally show a systematic increase when wind speed reached this value, and the direction range was selected to ensure that the PM$_{10}$ reaching the monitor was originating from within the dune preserve to the west of the station. The threshold WPD value for the summation procedure is 258 (W m^{-2}) based on the threshold windspeed of 7.5 m s^{-1}.

Similar to the network of stations already described, TPM$_{10}$ is positively and linearly corelated with the TWPD for each month of observation at the Oso Flaco monitoring site in 2019 and 2020. The mean monthly TPM$_{10}$:TWPD ratio for the period 2019 and 2020 is shown in Fig. 21. The temporal change pattern of the ratio suggests that there is no discernible trend in either of these years.

4. Discussion

4.1. 2013–2019 PI-SWERL measurements of emissivity

The mean emissivity relations shown in Fig. 9 for the available PI-SWERL emissivity data for the riding and non-riding areas covering the period 2013 to 2019, show that the riding-impacted areas of the ODSVRA have higher emissivity than all non-riding areas for equivalent values of u_*. This suggests, at the most general level of comparison, that riding augments emissivity of the sand dunes above that of the non-impacted sand dunes. At the lowest test u_* (0.38 m s^{-1}) emissivity of OHV-impacted sand is enhanced by a factor of 3.6 while at the higher value of 0.61 m s^{-1} it is enhanced by a factor of 1.9 (Fig. 9). The PI-SWERL test u_* values are approximately equivalent to 10 m AGL wind speeds of 10.0, 14.0 and 16.1 m s^{-1} (Mejia et al., 2019).

Within both riding and non-riding areas a north-south gradient of emissivity was observed, with higher emissivity in the north than in the south (Figs. 10 and 11). In the riding area the gradient of emissivity is linear (Fig. 11), and this is likely due to the increase in mean grain size of the sand from north to south. In unpublished data, Gillies and Etyemezian (2015) reported the mean grain diameter increased from ≈225 μm
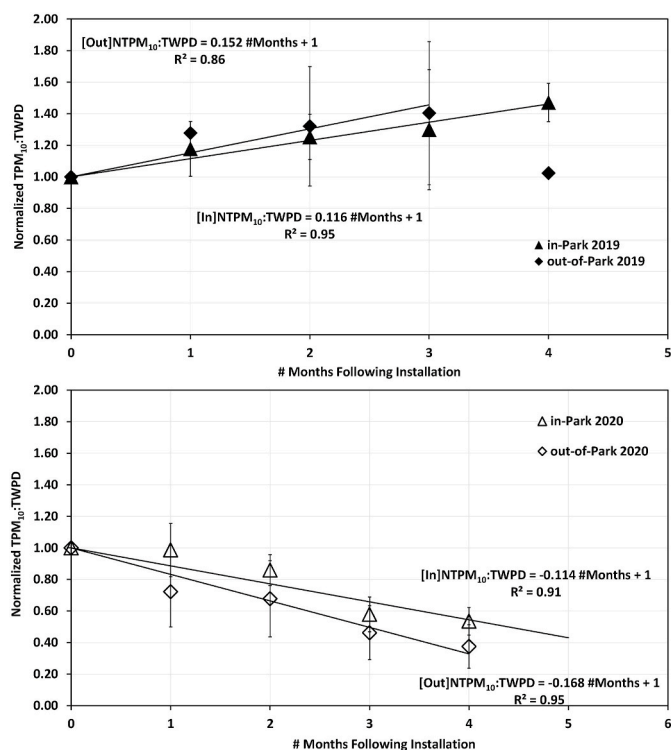
Fig. 19. Mean normalized TPM$_{10}$:TWPD ratio for all in-Park (triangle) and out-of-Park stations (diamond) as a function of number of months from installation for 2019 (top panel) and 2020 (bottom panel). The out-of-Park best-fit regression line for 2019 does not include the last month. Note x-axis is set at zero so the y-intercept can be set to one for the least squares regression. Error bars for both years represent the standard deviation of the mean normalized value for each month.
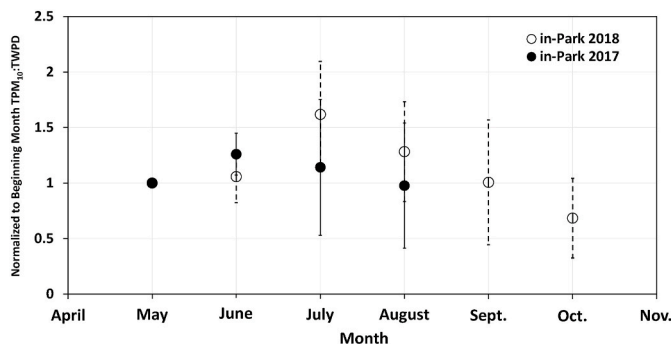

Fig. 20. Mean normalized TPM$_{10}$:TWPD ratio for all in-Park stations for the available record of May through September for 2017 and 2018. Error bars represent the standard deviation of the mean normalized value for each month.

in the north to ≈400 μm in the south over a distance of ≈8000 m. This north-south gradient of mean particle size is also present in the non-riding areas, and as Fig. 10 shows the non-riding areas also show a decrease in emissivity from north to south. Gillies and Etyemezian (2015) also reported that emissivity in the riding area of the ODSVRA, as measured with the PI-SWERL in 2013, increased with an increase in the proportion of the surface sand that was in the fine sand fraction (125–250 μm diameter).

The difference in emissivity between riding and non-riding does not appear to be much affected by latitudinal position in the ODSVRA as shown in Fig. 12. The degree of augmentation of emissivity due to vehicle impacts on the sand is approximately constant from north to south across the space of the ODSVRA. For u_* values well-above the
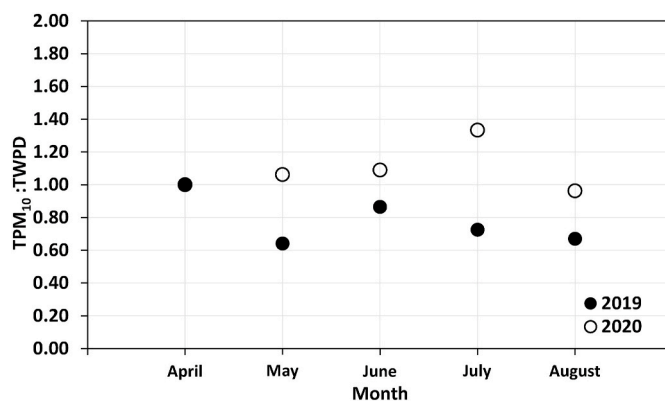

Fig. 21. The change in the mean monthly TPM$_{10}$:TWPD ratio at Oso Flaco, April to September 2019 and 2020.

threshold for saltation (>0.5 m s^{-1}), the riding area is between two to three times more emissive than non-riding areas at the same latitude (Fig. 12). This result agrees with Goossens et al. (2012) who report lower emissions on undisturbed sands than on OHV-disturbed sands at the Nellis Dunes OHV Recreation Area, Clark Co., NV. They also used a PI-SWERL to measure emissivity of riding and non-riding areas of this desert dune system to examine the ratio, emissivity in tracks in the sand: emissivity of non-OHV-impacted sand. The value of this ratio for dunes with no vegetation and dunes with vegetation are only provided by Goossens et al. (2012) in graphical format (their Fig. 11), which we interpret upon examination of their plot to be an augmentation of emissivity by a factor of between two to three.

4.2. PI-SWERL measurements, 2020

The repeated measurement of emissivity in the Lagrande Tract area in 2020, following the prohibition of OHV activity, was undertaken to determine if change could be observed with the passage of time. For the most part, these data are too variable to determine a time-dependent change in emissivity. The comparison of mean normalized emissivity of the Lagrande tract with the 2013–2019 mean emissivity of the riding and non-riding areas and the corresponding locations in the Lagrande Tract in 2019 (Fig. 3), shown in Fig. 15 by month, suggest that the 2020 Lagrande Tract monthly mean emissivity is lower than the long-term 2013–2019 emissivity of the ODSVRA riding area and the 2019 Lagrande Tract emissivity. The 2020 Lagrande Tract mean emissivity data are also greater than the long-term mean non-riding area emissivity for all months of observation.

Quantifying temporal change in the 2020 Lagrande Tract data is problematic due to the confounding influence of moisture effects that cannot be adequately controlled for. The simple filter applied to screen for gross moisture effects of precipitation is not sufficient to filter out the effects of very recent antecedent moisture inputs such as fog, and dew, and RH at the time of the measurements. It is well established that particle thresholds, sediment transport, and emissivity are sensitive to moisture (e.g., McKenna Neuman and Langston, 2006; McKenna Neuman, 2003; Ravi et al., 2004; Ravi and d'Odorico 2005; Nield and Wiggs, 2011). In the coastal environment of the ODSVRA moisture conditions of the sand change rapidly due to rapid changes in RH, solar radiation, cloud cover, etc., which affect moisture content at and near the surface of the sand making it challenging to account for their effects on PI-SWERL measured emissivity.

The 2020 PI-SWERL emissivity measurements in the Lagrande Tract provide a temporal record of emissivity for a large dust emission source, which has, to the best of our knowledge, only been done to limited degree and reported on in the literature (e.g., King et al., 2011; Cui et al., 2019). In most published research, measurements of emissivity made with the PI-SWERL are made at the location of interest only once, so

temporal variability of emissivity is not characterized. The variability of emissivity observed within the Lagrande Tract over seven months of monitoring, indicate that the dynamic nature of emissivity may be under-appreciated. The variability is likely increased in dynamic coastal environments such as the ODSVRA and lessens as the environment in which emissive surfaces are found becomes more stable.

4.3. PM concentration and wind data from the in-park monitors, 2017–2020

The meteorology and PM_{10} monitoring network data provide a more continuous record of the dust emission system across the spatial domain of the ODSVRA than can be obtained with periodic PI-SWERL measurements of emissivity. The instrument network enables characterization of the PM_{10} concentrations through a broad range of environmental conditions in which dust emissions occur. The measurements of meteorology and PM_{10} from 2017 to 2020, revealed that prior to 2020 the typical temporal pattern of change of the $TPM_{10}:TWPD$ ratio is a monthly increase beginning in spring/early summer reaching a maximum value in summer, and then a decline in the autumn, as exemplified by the data shown in Figs. 18 and 20.

The uniqueness of 2020 with its prohibition on OHV activity beginning in March, provided the opportunity to evaluate if the temporal change in the $TPM_{10}:TWPD$ ratio observed from 2017 to 2019 was a result of a natural process, or that it reflected an influence related to OHV activity. The data from 2020 suggest that following the cessation of riding there was a profound change in the dust emission system within the riding areas of the ODSVRA. The decrease in the $TPM_{10}:TWPD$ ratio observed in and exterior to the Park (Fig. 19), suggests that the influence of riding on emissions is observable and quantifiable. Combining the in-Park and out-of-Park station data shows that the production of PM_{10} during sustained periods of saltation decreased through time for equivalent TWPD conditions. The monthly change in the mean normalized $TPM_{10}:TWPD$ ratio for the stations within the riding area indicate that PM_{10} production from the wind-driven dune sands was decreasing by 11.6% per month following cessation of OHV activity across the ODSVRA. This decrease was also observed in the stations influenced by upwind riding areas, but the PM_{10} reaching these monitoring locations is a result of dispersion and not localized emissions.

Over the five months of monitoring, the decrease in total PM_{10} production as a function of total WPD decreased by 46.5% in the riding areas of the ODSVRA. This decrease suggests that OHV activity across the riding area increases the emissivity of the dune sands in agreement with the PI-SWERL measurements that compared emissivity of the riding and non-riding areas (Fig. 10). The $TPM_{10}:TWPD$ ratio as a function of month for the earlier data (2017–2019) suggest that OHV activity is, in part, responsible for the increase in PM_{10} production from spring through summer, augmenting dust production resulting from saltation processes by approximately 12% per month beginning in the spring and extending to autumn.

4.4. PM concentration and wind data from the Oso Flaco monitor, 2016–2020

The mean $TPM_{10}:TWPD$ ratio for the Oso Flaco monitoring site, for the April to August period in years 2019 and 2020, does not show evidence of an increase in production of PM_{10} from this area from spring to summer as observed for the riding area network stations in 2019 (Fig. 19), nor a decrease as observed in the 2020 data (Fig. 19). These Oso Flaco data (Fig. 21) suggest that the dust emission system in this non-OHV impacted part of the ODSVRA, was not influenced by a strong external forcing in these two years. The most likely environmental condition that influences dust emissions within the Oso Flaco area, after WPD, is the moisture regime, which will vary from month to month and year to year.

5. Conclusions

Two independent measurement methods for quantifying the emissivity of the dunes at the ODSVRA, one a direct measurement of surface emissivity (E, mg m^{-2} s^{-1}) obtained using the PI-SWERL instrument, and the second measuring wind power density (WPD, W m^{-2}) and airborne concentration of PM_{10} within the Park during periods of active emissions indicated that OHV activity augments the amount of PM_{10} produced by saltating dune sand. Generally, the emissivity as directly measured by the PI-SWERL in OHV-active and non-OHV areas indicates the augmentation is a factor of two to three times during periods well above the threshold for sand transport.

The measurements of WPD and PM_{10} concentrations at multiple monitoring locations interior and exterior to the ODSVRA, when expressed as monthly summations for all hours when WPD was ≥ 77 W m^{-2}, showed a strong linear dependence indicating WPD was an excellent quantity for relating the wind energy to the amount of PM_{10} produced by this saltation-driven dust emission system. The ratio $TPM_{10}:TWPD$ provided an index to track how the dust emission system changed temporally during years where OHV activity was allowed and for a span of time in 2020 when activity was prohibited due to the SARS-CoV-2 pandemic.

In years prior to 2020, PM_{10} originating from wind-driven saltation activity in the ODSVRA increased each month from spring to summer for the same WPD conditions, suggesting that cumulative OHV activity is the likely cause of the increase. In 2019, a year when OHV activity reflected a typical year, the monthly increase in the $TPM_{10}:TWPD$ ratio indicated the augmentation was approximately 12% per month beginning in spring. In 2020, when OHV activity was prohibited, data collected from April through August indicated that the $TPM_{10}:TWPD$ ratio declined linearly by approximately 12% per month indicating that the dust emission system was moving to a lower state of emissivity in the absence of impacts created by OHV activity. The temporal change in the mean $TPM_{10}:TWPD$ ratio for two years of monitoring at Oso Flaco exhibited a pattern unlike those observed for stations in the ODSVRA and immediately exterior and downwind of riding areas.

This analysis does not reveal the mechanisms responsible for the augmentation of dust emissions by OHV activity at the ODSVRA. The data from two separate measurement methods and the presented analyses both support that the effect is demonstrable, and the magnitude of the augmentation is quantified for the ODSVRA in terms of emissivity of the surface and PM_{10} concentration observed within and exterior to the park. The rate of change of the $TPM_{10}:TWPD$ ratio suggest that the dust emission system in 2020 (Fig. 19) was moving towards a new emissive state. We suggest that this is due to multiple changes principally as it relates to the sand surface including: the cessation of vehicle-induced abrasion mechanisms, a coarsening of the surface sand due to a winnowing effect, and an increase in surface topography complexity as bedforms evolve in the absence of vehicle disturbance. Since a historical record of wind, PM concentrations, or surface emissivity that extends back to before the dunes were impacted by OHV activity does not exist, it is difficult to say when the dunes would achieve a state representative of a pre-OHV impact condition.

The best proxy condition to consider for representing the current riding area as non-OHV-impacted may be to use the non-riding area emissivity relations (Figs. 9 and 10) as input into an emission and dispersion model, such as one described by Mejia et al. (2019). This type of model could be used to estimate PM_{10} concentrations at downwind receptor sites under a no-OHV activity scenario. This could provide important information for developing a management strategy to reduce the PM_{10} generated in the ODSVRA that impacts downwind receptors and the people who live in the area by setting a target emissions reduction that represents something close to the baseline condition of a non-OHV impacted Oceano dune system.

CRediT authorship contribution statement

J.A. Gillies: Conceptualization, Methodology, Investigation, Analysis, Writing – original draft. **E. Furtak-Cole:** Investigation, Analysis, Reviewing. **G. Nikolich:** Methodology, Investigation, Analysis, Reviewing. **V. Etyemezian:** Conceptualization, Methodology, Investigation, Reviewing.

Declaration of competing interest

The authors declare that they have no known competing financial interests or personal relationships that could have appeared to influence the work reported in this paper.

Acknowledgements

References

Bagnold, R.A., 1941. The Physics of Blown Sand and Desert Dunes. Chapman and Hall, London.

Bristow, C.S., Moller, T.H., 2018. Testing the auto-abrasion hypothesis for dust production using diatomite dune sediments from the Bodele depression in Chad. Sedimentology 65, 1322–1330.

Bullard, J.E., McTainsh, G.H., Pudmenzky, C., 2004. Aeolian abrasion and modes of fine particle production from natural red dune sands: an experimental study. Sedimentology 51, 1103–1125.

Bullard, J.E., McTainsh, G.H., Pudmenzky, C., 2007. Factors affecting the rate and nature of fine particle production by aeolian abrasion. Sedimentology 54, 1169–1182.

Bullard, J.E., White, K., 2005. Dust production and the release of iron oxides resulting from the aeolian abrasion of natural dune sands. Earth Surf. Process. Landforms 30, 95–106.

Chepil, W.S., 1945. Dynamics of wind erosion: III. The transport capacity of the wind. Soil Sci. 60, 475–480.

Cui, M.C., Lu, H., Wiggs, G.F.S., Etyemezian, V., Sweeney, M.R., Xu, Z.W., 2019. Quantifying the effect of geomorphology on aeolian dust emission potential in northern China. Earth Surf. Process. Landforms 44, 2872–2884.

Etyemezian, V., Gillies, J.A., Shinoda, M., Nikolich, G., King, J., Bardis, A.R., 2014. Accounting for surface roughness on measurements conducted with PI-SWERL: evaluation of a subjective visual approach and a photogrammetric technique. Aeolian Res. 13, 35–50.

Etyemezian, V., Nikolich, G., Ahonen, S., Pitchford, M., Sweeney, M., Gillies, J., Kuhns, H., 2007. The Portable In-Situ Wind Erosion Laboratory (PI-SWERL): a new method to measure PM_{10} windblown dust properties and potential for emissions. Atmos. Environ. 41, 3789–3796.

Gillies, J.A., Etyemezian, V., 2015. Addendum to the PI-SWERL Report of Etyemezian et al. (2014) Particle Size Distribution Characteristics and PI-SWERL PM_{10} Emission Measurements: Oceano Dunes State Vehicular Recreation Area. Report prepared by the Desert Research Institute for Off-Highway Motor Vehicular Recreation Division, California State Parks, 1725 23rd Street, Suite 200, Sacramento, CA 95816, July 13, 2015 (available upon request).

Gillies, J.A., Etyemezian, V., Nikolich, G., Glick, R., Rowland, P., Pesce, T., Skinner, M., 2017. Effectiveness of an array of porous fences to reduce sand flux: Oceano Dunes, Oceano CA. J. Wind Eng. Ind. Aerod. 168, 247–259.

Goossens, D., Buck, B., 2009a. Dust dynamics in off-road vehicle trails: measurements on 16 arid soil types, Nevada. J. Environ. Manag. 90, 3458–3469.

Goossens, D., Buck, B., 2009b. Dust emission by off-road driving: experiments on 17 arid soil types, Nevada, USA. Geomorphology 107, 118–138.

Goossens, D., Buck, B., 2011. Effects of wind erosion, off-road vehicular activity, atmospheric conditions and the proximity of a metropolitan area on PM_{10} characteristics in a recreational area. Atmos. Environ. 45, 94–107.

Goossens, D., Buck, B., McLaurin, B., 2012. Contributions to atmospheric dust production of natural and anthropogenic emissions in a recreational area designated for off-road vehicular activity (Nellis Dunes, Nevada, USA). J. Arid Environ. 78, 80–99.

Hagen, L.J., Wagner, L.E., Skidmore, E.L., 1999. Analytical solutions and sensitivity analyses for sediment transport in WEPS. Trans. ASAE (Am. Soc. Agric. Eng.) 42, 1715–1721.

Huang, Y., Kok, J.F., Martin, R.L., Swet, N., Katra, I., Gill, T.E., Reynolds, R.L., Freire, L. S., 2019. Fine dust emissions from active sands at coastal Oceano Dunes, California. Atmos. Chem. Phys. 19, 2947–2964.

Kalmikov, A., 2017. Wind power fundamentals. In: Letcher, T.M. (Ed.), Wind Power Engineering. Elsevier Science Publishing Co., Inc.

King, J., Etyemezian, V., Sweeney, M., Buck, B.J., Nikolich, G., 2011. Dust emission variability at the Salton Sea, California, USA. Aeolian Res. 3, 67–79.

Kuenen, P.H., 1960. Experimental abrasion 4: eolian action. J. Geol. 68, 427–449.

McKenna Neuman, C., 2003. Effects of temperature and humidity upon the entrainment of sedimentary particles by wind. Boundary-Layer Meteorol. 108, 61–89.

McKenna Neuman, C., Langston, G., 2006. Measurement of water content as a control of particle entrainment by wind. Earth Surf. Process. Landforms 31, 303–317.

Mejia, J.F., Gillies, J.A., Etyemezian, V., Glick, R., 2019. A very-high resolution (20m) measurement-based dust emissions and dispersion modeling approach for the Oceano Dunes, California. Atmos. Environ. 218.

Nield, J.M., Wiggs, G.F.S., 2011. The application of terrestrial laser scanning to aeolian saltation cloud measurement and its response to changing surface moisture. Earth Surf. Process. Landforms 36, 273–278.

Orme, A.R., Tchakerian, V.P., 1986. Quaternary dunes of the Pacific coast of the California. In: Nickling, W.G. (Ed.), Aeolian Geomorphology. Allen and Unwin, Boston, London, Sydney, pp. 149–175.

Ravi, S., D'Odorico, P., 2005. A field-scale analysis of the dependence of wind erosion threshold velocity on air humidity. Geophys. Res. Lett. 32.

Ravi, S., D'Odorico, P., Over, T.M., Zobeck, T.M., 2004. On the effect of air humidity on soil susceptibility to wind erosion: the case of air-dry soils. Geophys. Res. Lett. 31.

Skidmore, E.L., 1998. Wind erosion processes. In: Sivakumar, M.V.K., Zbisch, M.A., Koala, S., Maukonen, T. (Eds.), Wind Erosion in Africa and West Asia: Problems and Strategies. International Center for Agricultural Research in Dry Areas (ICARDA), Aleppo, pp. 137–142.

Swet, N., Elperin, T., Kok, J.F., Martin, R.L., Yizhaq, H., Katra, I., 2019. Can active sands generate dust particles by wind-induced processes? Earth Planet Sci. Lett. 506, 371–380. https://doi.org/10.1016/j.epsl.2018.11.013.

Swet, N., Kok, J.F., Huang, Y., Yizhaq, H., Katra, I., 2020. Low dust generation potential from active sand grains by wind abrasion. J. Geophys. Res.: Earth Surface 125, e2020JF005545.

von Holdt, J.R.C., Eckardt, F.D., Baddock, M.C., Wiggs, G.F.S., 2019. Assessing landscape dust emission potential using combined ground-based measurements and remote sensing data. J. Geophys. Res.: Earth Surface 124, 1080–1098.

Wilshire, H.G., Nakata, J.K., 1976. Off-road vehicle effects on California's Mojave Desert. Calif. Geol. 29, 123–132.